
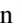












# Stellar and Planetary Characterization of the Ross 128 Exoplanetary System from APOGEE Spectra

Diogo Souto<sup>1</sup> , Cayman T. Unterborn<sup>2</sup> , Verne V. Smith<sup>3</sup>, Katia Cunha<sup>1,4</sup>, Johanna Teske<sup>5,6,18</sup>, Kevin Covey<sup>7</sup> ,  
Bárbara Rojas-Ayala<sup>8</sup>, D. A. García-Hernández<sup>9,10</sup>, Keivan Stassun<sup>11,12</sup> , Olga Zamora<sup>9,10</sup>, Thomas Masseron<sup>9,10</sup>,  
J. A. Johnson<sup>13</sup> , Steven R. Majewski<sup>14</sup> , Henrik Jönsson<sup>15</sup> , Steven Gilhool<sup>16</sup> , Cullen Blake<sup>16</sup> , and Felipe Santana<sup>17</sup> 

<sup>1</sup> Observatório Nacional, Rua General José Cristino, 77, 20921-400 São Cristóvão, Rio de Janeiro, RJ, Brazil; [souto@on.br](mailto:souto@on.br), [diogodusouto@gmail.com](mailto:diogodusouto@gmail.com)

<sup>2</sup> School of Earth and Space Exploration, Arizona State University, Tempe, AZ 85287, USA

<sup>3</sup> National Optical Astronomy Observatory, 950 North Cherry Avenue, Tucson, AZ 85719, USA

<sup>4</sup> Steward Observatory, University of Arizona, 933 North Cherry Avenue, Tucson, AZ 85721-0065, USA

<sup>5</sup> Department of Terrestrial Magnetism, Carnegie Institution for Science, Washington, DC 20015, USA

<sup>6</sup> The Observatories of the Carnegie Institution for Science, 813 Santa Barbara Street, Pasadena, CA 91101, USA

<sup>7</sup> Department of Physics & Astronomy, Western Washington University, Bellingham, WA 98225, USA

<sup>8</sup> Departamento de Ciencias Físicas, Universidad Andres Bello, Fernandez Concha 700, Las Condes, Santiago, Chile

<sup>9</sup> Instituto de Astrofísica de Canarias, E-38205 La Laguna, Tenerife, Spain

<sup>10</sup> Departamento de Astrofísica, Universidad de La Laguna, E-38206 La Laguna, Tenerife, Spain

<sup>11</sup> Department of Physics and Astronomy, Vanderbilt University, 6301 Stevenson Center Ln., Nashville, TN 37235, USA

<sup>12</sup> Department of Physics, Fisk University, 1000 17th Ave. N., Nashville, TN 37208, USA

<sup>13</sup> Department of Astronomy, The Ohio State University, Columbus, OH 43210, USA

<sup>14</sup> Department of Astronomy, University of Virginia, Charlottesville, VA 22904-4325, USA

<sup>15</sup> Lund Observatory, Department of Astronomy and Theoretical Physics, Lund University, Box 43, SE-221 00 Lund, Sweden

<sup>16</sup> Department of Physics and Astronomy, University of Pennsylvania, 209 S. 33rd Street, Philadelphia, PA 19104, USA

<sup>17</sup> Universidad de Chile, Av. Libertador Bernardo OHiggins 1058, Santiago De Chile, Chile

Received 2018 May 11; revised 2018 May 27; accepted 2018 May 28; published 2018 June 13

## Abstract

The first detailed chemical abundance analysis of the M-dwarf (M4.0) exoplanet-hosting star Ross 128 is presented here, based upon near-infrared (1.5–1.7  $\mu\text{m}$ ), high-resolution ( $R \sim 22,500$ ) spectra from the SDSS Apache Point Galactic Evolution Experiment survey. We determined precise atmospheric parameters  $T_{\text{eff}} = 3231 \pm 100$  K,  $\log g = 4.96 \pm 0.11$  dex and chemical abundances of eight elements (C, O, Mg, Al, K, Ca, Ti, and Fe), finding Ross 128 to have near solar metallicity ( $[\text{Fe}/\text{H}] = +0.03 \pm 0.09$  dex). The derived results were obtained via spectral synthesis (1D LTE) adopting both MARCS and PHOENIX model atmospheres; stellar parameters and chemical abundances derived from the different adopted models do not show significant offsets. Mass–radius modeling of Ross 128b indicates that it lies below the pure-rock composition curve, suggesting that it contains a mixture of rock and iron, with the relative amounts of each set by the ratio of Fe/Mg. If Ross 128b formed with a subsolar Si abundance, and assuming the planet’s composition matches that of the host star, it likely has a larger core size relative to the Earth despite this producing a planet with a Si/Mg abundance ratio  $\sim 34\%$  greater than the Sun. The derived planetary parameters—insolation flux ( $S_{\text{Earth}} = 1.79 \pm 0.26$ ) and equilibrium temperature ( $T_{\text{eq}} = 294 \pm 10$  K)—support previous findings that Ross 128b is a temperate exoplanet in the inner edge of the habitable zone.

**Key words:** stars: abundances – infrared: stars – planet–star interactions – planetary systems – stars: fundamental parameters – stars: low-mass

## 1. Introduction

Nearby M dwarfs likely provide some of the best opportunities for detecting and characterizing potentially “Earth-like” exoplanets in the near future. M dwarfs produce larger observational signatures from low-mass exoplanets through both the radial velocity (RV) and transit methods (Charbonneau & Deming 2007; Shields et al. 2016), making it easier to discover Earth-size or Earth-mass exoplanets orbiting these stars. Discoveries of Earth-size or Earth-mass exoplanets have become common around low-mass stars thanks to the efforts of high-cadence radial velocity programs, as well as the *Kepler* mission (Batalha et al. 2013). Proxima Cen b and the recent announcement of Ross 128b are examples of RV-detected exoplanets (Anglada-Escudé et al. 2016, Bonfils et al. 2017), while TRAPPIST-1, Kepler-138, and Kepler-186 (Quintana et al. 2014; Jontof-Hutter et al. 2015; Gillon et al.

2017; Souto et al. 2017) are examples of transiting exoplanet systems with cool M-dwarf host stars.

An approach to study the exoplanet composition, albeit an indirect one, is the analysis of the individual host star. This method can, for example, provide measurements of a star’s C and O abundance, which play a role in the ice and gas chemistry in protoplanetary disks, as well as Mg, Fe, and Si abundances, that potentially control a rocky planet’s core to mantle mass ratios (Bond et al. 2010; Delgado Mena et al. 2010; Thiabaud et al. 2015; Dorn et al. 2017; Santos et al. 2017, and Unterborn & Panero 2017). Until recently, detailed abundance measurements of M dwarfs were lacking, due in part to the difficulty of obtaining high-S/N, high-resolution spectra, as well as strong molecular absorption from species such as TiO in the optical or H<sub>2</sub>O in the near-infrared (Allard et al. 2013).

The previous work of Souto et al. (2017) demonstrated that effective temperatures and detailed individual abundances of 13 elements can be measured from near-infrared (NIR) H-band

<sup>18</sup> Hubble Fellow.

high-resolution Apache Point Galactic Evolution Experiment (APOGEE; Majewski et al. 2017) spectra of warm M dwarfs ( $T_{\text{eff}} \sim 3900$  K; see also Schmidt et al. 2016). Also using high-resolution spectra, Önehag et al. (2012) and Lindgren & Heiter (2017) have shown that stellar metallicities can be studied from J-band spectra. Most studies, however, use photometric calibrations to determine M-dwarf stellar parameters, e.g.,  $T_{\text{eff}}$ ,  $\log g$ , and mass (Delfosse et al. 2000; Bonfils et al. 2005; Mann et al. 2015) and low-resolution NIR spectroscopy to determine M-dwarf metallicities ( $[\text{Fe}/\text{H}]$ ) from equivalent widths in the K band (Rojas-Ayala et al. 2012). These methods provide a good estimate of the stellar parameters and metallicity; in the context of exoplanet studies, accurate values for  $T_{\text{eff}}$  and  $R_*$  are needed in order to better constrain the exoplanet properties (e.g., insolation, equilibrium temperature). In addition, precise host star abundance measurements for particular elements can help to constrain the composition of the initial refractory materials that build rocky exoplanets.

In this work, we perform the first detailed abundance analysis for Ross 128, a cool M-dwarf (M4.0) exoplanet host. We use  $R \sim 22,500$  H-band APOGEE spectra to derive precise atmospheric parameters and chemical abundances of eight elements adopting a similar methodology as Souto et al. (2017), but extending the analysis to the cool M-dwarf regime. Such parameters are needed to better characterize the mass ( $M \sin(i) \sim 1.35 M_{\oplus}$ ) of the 9.9 day period exoplanet around Ross 128, the second closest (3.37 pc) terrestrial-mass planet, recently discovered by Bonfils et al. (2017).

## 2. Observations and Spectrum Synthesis

The APOGEE survey (Majewski et al. 2017; see also Blanton et al. 2017; Zasowski et al. 2017) observes primarily red giants, but has also observed M dwarfs in the solar neighborhood to fill missing fibers or as part of ancillary projects. With APOGEE NIR spectral coverage ( $\lambda 15,150\text{--}17,000$  Å) and high-resolution spectroscopic capabilities (Gunn et al. 2006; Wilson et al. 2010), the APOGEE spectrograph has turned out to be an excellent instrument for detailed studies of M dwarfs (see Souto et al. 2017).

The APOGEE spectra of Ross 128 (HIP 57548; GJ 447; 2M11474440+0048164) were obtained with the fiber feed to the NMSU 1.0 m telescope at APO. We use the processed spectrum of Ross 128 from the DR14 pipeline (Nidever et al. 2015; Abolfathi et al. 2018) representing the combination of two individual observations both obtained on 2014 January 28. The resulting S/N (per pixel) in the combined spectrum is 230.

As a first step in the analysis we conducted a careful identification of the main spectral features in the APOGEE spectrum of Ross 128, given that this is a much cooler M dwarf than those previously analyzed in Souto et al. (2017). Figure 1 displays the molecular and atomic lines identified; in this  $T_{\text{eff}}$  regime most of the APOGEE spectrum is dominated by  $\text{H}_2\text{O}$  or FeH lines but some atomic lines of Fe I, Mg I, Ca I, and Al I are also seen. We performed a line-by-line manual abundance analysis to determine the atmospheric parameters of Ross 128 (Section 2.1) and individual chemical abundances of the elements C, O, Mg, Al, K, Ca, Ti, and Fe. The adopted transitions in the line-by-line abundance analysis (a total of 86 lines) are indicated with black vertical tick marks in Figure 1. Figure 1 also shows the best-fit synthetic spectra obtained from this analysis, as discussed below.

A spectrum synthesis analysis is required to analyze cool star (M-dwarf) spectra, rather than the equivalent-width method, due to molecular blends that blanket their spectra. In this work, we adopted 1D plane-parallel LTE models from MARCS and BT-Settl PHOENIX (Gustafsson et al. 2008; Allard et al. 2013). The synthetic spectra were computed with the Turbospectrum code (Alvarez & Plez 1998; Plez 2012) using the modified version of the APOGEE line list (Shetrone et al. 2015; Souto et al. 2017) that takes into account transitions of FeH. The synthetic spectra were broadened with a Gaussian profile corresponding to the APOGEE resolution (FWHM  $\sim 0.73$  Å). We derived a  $v \sin i \leq 8$  km s $^{-1}$  for Ross 128 and note that this  $v \sin i$  value is at the limit of what can be resolved from APOGEE spectra Gilhool et al. (2018). In all calculations, we adopted a microturbulent velocity of  $\xi = 1.00$  km s $^{-1}$ . The best-fit synthetic spectra were obtained by defining the pseudo-continuum of the observed spectra over each window analyzed, and the derived abundances are the value best fitting the observed spectra from a  $\chi^2$ -minimization method.

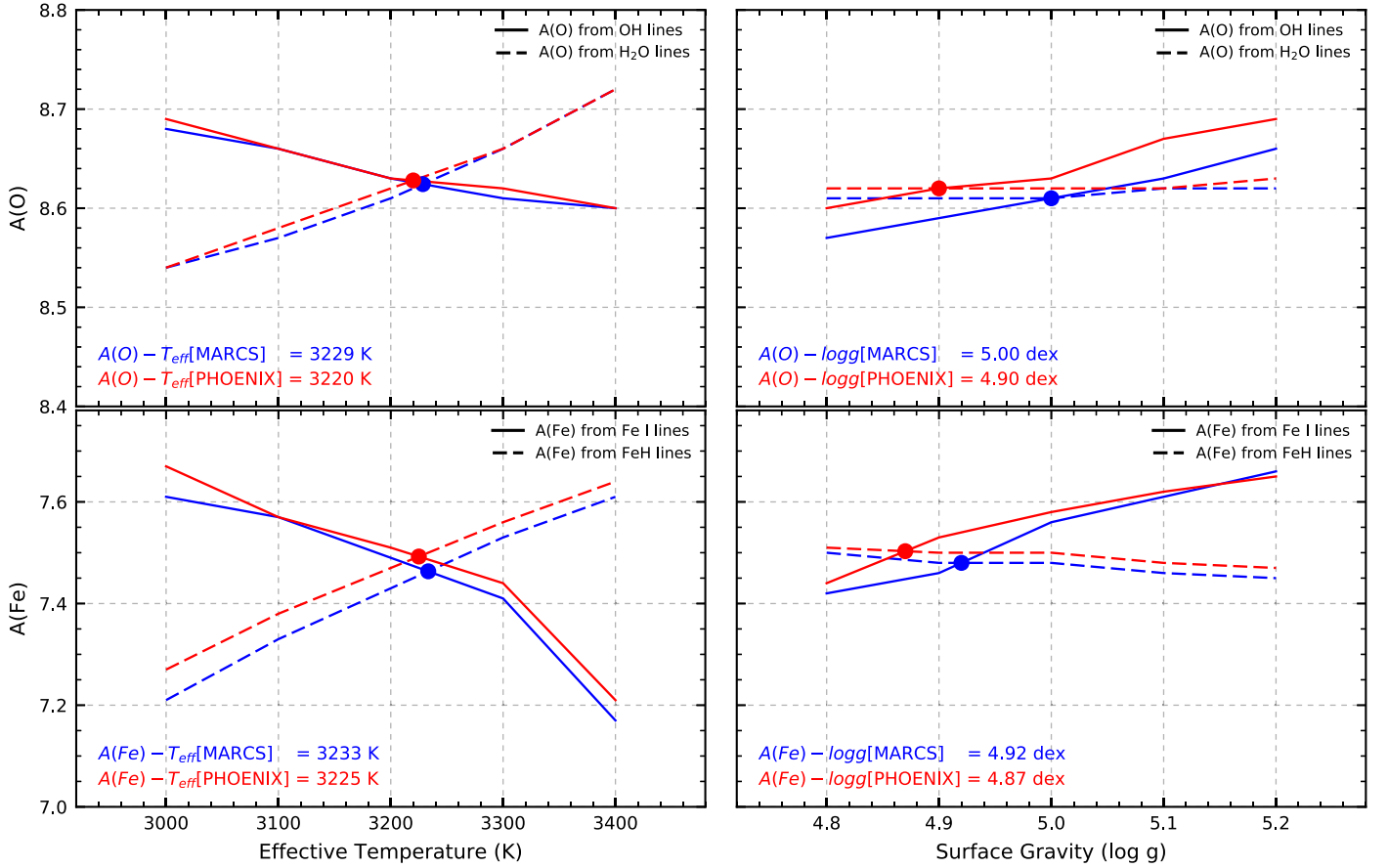
### 2.1. Effective Temperature and Surface Gravity

The effective temperature ( $T_{\text{eff}}$ ) and surface gravity ( $\log g$ ) values of Ross 128 were obtained using a similar methodology as discussed in Souto et al. (2017). That previous study used the OH and  $\text{H}_2\text{O}$  lines as oxygen abundance indicators to define the effective temperature. Here, we add Fe I and FeH as Fe abundance indicators and use the combination of oxygen and iron abundances from OH,  $\text{H}_2\text{O}$ , Fe I, and FeH for deriving both the effective temperature and the surface gravity for Ross 128.

Figure 2 shows the derived oxygen and iron abundances as functions of  $T_{\text{eff}}$  and  $\log g$  for both MARCS and PHOENIX model atmospheres. The effective temperature and  $\log g$  are defined by the agreement between the different abundance indicators (crossing points). The derived effective temperature using the  $T_{\text{eff}}\text{--}A(\text{O})$  pair (top left panel) is quite similar to the one from the  $T_{\text{eff}}\text{--}A(\text{Fe})$  pair (bottom left panel), with a  $T_{\text{eff}}$  difference of only  $\sim 5$  K; a similar effective temperature is derived using either family of model atmosphere. The same is true for  $\log g$ , although with slightly larger differences ( $\sim 0.02\text{--}0.08$  dex). These results indicate that good consistency can be obtained between the different abundance indicators.

The stellar parameters and individual abundances derived from MARCS and PHOENIX models are very similar (Tables 1 and 2). We derive  $T_{\text{eff}} = 3231/3223 \pm 100$  K,  $\log g = 4.96/4.89 \pm 0.11$  dex, and  $[\text{Fe}/\text{H}] = +0.03/+0.04 \pm 0.09$  (MARCS/PHOENIX). The uncertainties in  $T_{\text{eff}}$  and  $\log g$  were estimated by allowing the Fe abundances from Fe I and FeH lines and oxygen abundances from  $\text{H}_2\text{O}$  and OH lines to differ by 0.1 dex. The values from Rojas-Ayala et al. (2012) displayed in Table 1 were obtained using the same techniques as Muirhead et al. (2014). We adopt the  $V\text{--}J$  and  $r\text{--}J$  colors to determine the  $T_{\text{eff}}$  from Mann et al. (2015). The derived surface gravity ( $\log g = 4.96$ ) agrees well with the  $\log g$  obtained from the physical relation ( $\log g = 5.09$ ) assuming  $M_* = 0.168 \pm 0.017 M_{\odot}$  from Mann et al. (2015),  $L = 0.00367 L_{\odot}$  from Gaia DR2 (Gaia Collaboration et al. 2018), and the  $T_{\text{eff}}$  of this work using the MARCS model, where  $T_{\text{eff},\odot} = 5772$  K and  $\log g_{\odot} = 4.438$  were adopted. Table 2 presents the abundance results, the standard deviation of the mean abundances from the adopted lines (std), and the abundance uncertainties for each species ( $\sigma$ ) to changes in the atmospheric parameters (computed following Souto et al. 2017).





**Figure 2.** Diagrams illustrating the derivation of atmospheric parameters. The left panels display the  $T_{\text{eff}}-A(\text{O})$  and  $T_{\text{eff}}-A(\text{Fe})$  curves and the right panels the  $\log g-A(\text{O})$  and  $\log g-A(\text{Fe})$  pairs. In all panels, the derived abundances from Fe I and OH lines are shown as solid lines, while those from FeH and H<sub>2</sub>O as dashed lines. The different colors (blue and red) indicate results derived from the adopted models, MARCS and PHOENIX, respectively.

**Table 1**  
Atmospheric Parameters

	$T_{\text{eff}}$	$\log g$	$\xi$	[Fe/H]	[O/H]
MARCS	$3231 \pm 100$	$4.96 \pm 0.11$	1.00	+0.02	-0.03
PHOENIX	$3223 \pm 100$	$4.89 \pm 0.11$	1.00	+0.03	-0.02
Rojas-Ayala et al. (2012)	$2986 \pm 50$	...	...	+0.03	...
Mann et al. (2015)	$3192 \pm 64$	5.08	...	-0.02	...

provide some broad constraints on the possible structures of Ross 128b.

While both mass and radius are not available for Ross 128b, we can estimate its radius given its observed minimum mass and assuming the stellar composition of the host star is a proxy for that of the planet. We calculate the range of radii possible for Ross 128b using the ExoPlex software package (Unterborn et al. 2018) for all masses above the minimum mass of Ross 128b ( $1.35 M_{\oplus}$ ; Bonfils et al. 2017). Models were run assuming a two-layer model with a liquid core and silicate mantle (no atmosphere). We increase the input mass until a likely radius of  $1.5 R_{\oplus}$  was achieved, roughly the point where planets are not expected to be gas-rich mini-Neptunes as opposed to rock and iron-dominated super-Earths (Figure 3, left). ExoPlex conserves the relative molar ratios for the dominant rocky planet-building elements assuming all Fe is present in the core with no light elements (e.g., Si, O, H) present in the core. Adopting our

MARCS abundances we get the molar ratios  $\text{Fe}/\text{Mg} = 1.12$ ,  $\text{Ca}/\text{Mg} = 0.09$ , and  $\text{Al}/\text{Mg} = 0.08$ , where the Earth and solar values are 0.90/0.07/0.09 (McDonough 2003) and 0.83/0.06/0.08 (Lodders 2003), respectively.

Changes in the relative planet's core size have a large effect on its bulk density (Unterborn et al. 2016), and we thus consider our Fe abundance uncertainty:  $0.88 \leq \text{Fe}/\text{Mg} \leq 1.3$ . We also varied Si/Mg between the extremes of 0.5 and 2 (Solar Si/Mg is 0.97). This range of Si/Mg represents an average difference in radius for a given input mass of roughly  $0.05 R_{\oplus}$  (Figure 3, left panel). However, because the molar mass of MgO is 1/3 smaller than SiO<sub>2</sub> (our chosen mantle oxides), this range of Si/Mg represents core mass fractions between 0.44 and 0.27 (Earth is 0.33) for Si/Mg of 0.5 and 2, respectively. For this model, only if Ross 128b had a supersolar Si/Mg of 1.3 would it match the Earth in its core mass fraction, which equates to Ross 128 having a Si abundance of roughly solar ( $A(\text{Si}) = 7.54$ ). That is to say while the molar ratio of Fe/Mg is conserved, the mass ratio of Fe/Mg in our model is not and depends on the chosen Mg/Si. This means that if Ross 128b's composition mimics that of its host star and a subsolar Si/Mg, it will have a larger relative core size than Earth, despite having roughly solar iron abundance. This is due to the relative ratio of Fe to Mg being greater than in the Sun and Earth, combined with the density of liquid Fe being greater than that of magnesium silicates (e.g., rock dominated). We note that the uncertainty in the derived radii is about the size of the red curve in Figure 3 (left panel).

**Table 2**  
Individual Abundances

	MARCS			PHOENIX			Number of Lines	$\sigma$
A(X)	[X/H]	std	A(X)	[X/H]	std			
Fe I	7.48	0.03	0.02	7.49	0.04	0.02	2	0.09
FeH	7.45	0.00	0.07	7.46	0.01	0.08	30	0.08
C	8.41	0.02	0.01	8.41	0.02	0.01	3	0.02
OH	8.62	-0.04	0.02	8.63	-0.03	0.02	29	0.06
H <sub>2</sub> O	8.64	-0.02	0.02	8.64	-0.02	0.03	10	0.08
Mg	7.43	-0.10	...	7.48	-0.05	...	1	0.13
Al	6.35	-0.02	...	6.36	-0.01	...	1	0.10
K	5.03	-0.05	0.03	5.06	-0.02	0.03	2	0.04
Ca	6.36	-0.01	0.02	6.38	0.01	0.03	2	0.03
Ti	4.73	-0.17	0.21	4.77	-0.13	0.20	6	0.09

Our calculated Ross 128b radii—under the assumption that the stellar chemical abundances are also those in the planet—all lie below the 100% rock composition curve of Zeng et al. (2016), i.e., it contains a mixture of rock and Fe, with the relative amounts of each set by Fe/Mg. Given our compositional constraints, these calculated radii represent the *minimum* radius of Ross 128b in the absence of collisional stripping of silicate relative to iron (see also Benz et al. 1988; Marcus et al. 2010). This means that the addition of light elements to the core or the presence of surface water or an atmosphere will only lower the planet density, causing a radius increase for the same mass. The Ross 128b relatively Fe-rich composition may affect its geodynamo (Gaidos et al. 2010; Driscoll & Olson 2011), although the geodynamic and geochemical consequences of Fe-rich planets are not well explored.

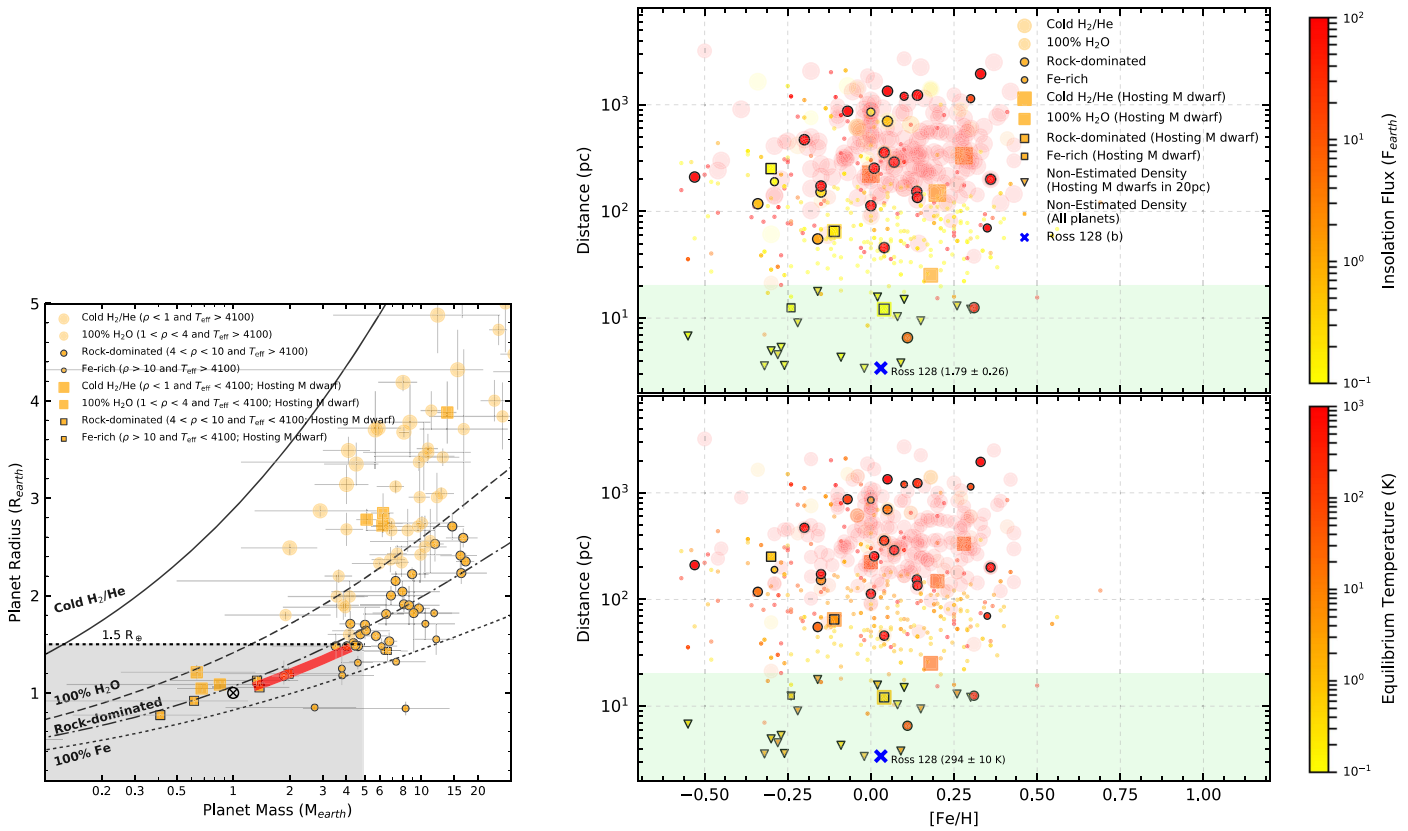
With the results presented here, we can study some Ross 128b fundamental habitability parameters such as insolation flux ( $S_{\text{Earth}}$ ; flux of energy the exoplanet receives from its host star) and equilibrium temperature ( $T_{\text{eq}}$ ). Bonfils et al. (2017) predict that Ross 128b should have an insolation flux ( $S_{\text{Earth}}$ ) of 1.38. Adopting our MARCS  $T_{\text{eff}}$ , the stellar radius ( $R_* = 0.209 \pm 0.002 R_{\odot}$ ; very similar to Mann et al. 2015) derived by us from the spectral energy distribution (Stassun et al. 2017) and adopting the Bonfils et al. (2017) semimajor axis (SMA = 0.049 au), we derive  $S_{\text{Earth}} = 1.79 \pm 0.26$  for Ross 128b, which is consistent with Bonfils et al. (2017). The  $T_{\text{eq}}$  of an exoplanet is a function of the stellar  $T_{\text{eff}}$ , radius, the SMA of the planet and its albedo. We obtain for Ross 128b a  $T_{\text{eq}} = 294 \pm 10$  K for an Earth-like albedo (0.306). Adopting a Venus- and Mars-like albedo (0.77 and 0.25), we derive a  $T_{\text{eq}}$  of  $223 \pm 0.08$  and  $299 \pm 11$  K, respectively. Our results support the claim of Bonfils et al. (2017) that Ross 128b is a temperate exoplanet in the inner edge of the habitable zone. However, this is not to say that Ross 128b is a “Exo-Earth.” Geologic factors unexplored in Bonfils et al. (2017) such as the planet’s likelihood to produce continental crust, the weathering rates of key nutrients into ocean basins, or the presence of a long-term magnetic field could produce a planet decidedly not at all “Earth-like” or habitable due to differences in its composition and thermal history. Furthermore, other aspects of the M dwarf’s stellar activity and its effect on the retention of any atmosphere and potential habitability should be studied, although we find no evidence of activity in the Ross 128 spectra.

In Figure 3, we use the NASA Exoplanet Archive to study the planetary density (left panel), the metallicity distribution of the host stars as well as the insolation flux and the planet

equilibrium temperature as a function of the distance of the systems to the Sun (right panels). We split the sample of known exoplanets into four groups based on the mass–radius bulk-composition curves from Zeng et al. (2016). The planets with density ( $\rho$ ) < 1 were tagged as Cold H<sub>2</sub>/He, where  $1 < \rho < 4$  have a predominant H<sub>2</sub>O atmosphere, the rock-dominated exoplanets have  $4 < \rho < 10$ , and those with  $\rho > 10$  are tagged as Fe-rich exoplanets; we did not take density errors into account for these rough categories. To give particular attention to the M dwarfs hosting exoplanets, we split the sample into stars with  $T_{\text{eff}} < 4100$  K (squared symbols) and  $T_{\text{eff}} > 4100$  K (circled symbols) using the same cuts in density. In Figure 3 (left panel), likely rocky exoplanets are highlighted and the gray shadow region indicates the potential regime for Earth-like exoplanets (with radii from 0 to  $1.5 R_{\oplus}$  and masses from 0 to  $5 M_{\oplus}$ ). The estimated radii for Ross 128b are displayed as a solid red line. The size of the red line represents the typical uncertainty in the estimated radii.

We show in the right panel of Figure 3 the metallicity ([Fe/H]) distance (pc) distribution of the host stars, with the exoplanet insolation flux (Figure 3, top right panel) and equilibrium temperature (Figure 3, bottom right panel) represented by color bars. We compute the exoplanet insolation flux and the equilibrium temperature using the  $T_{\text{eff}}$ ,  $R_*$ , and SMA from the NASA Exoplanet Archive with an Earth-like albedo (30%) for all exoplanets. For the M dwarfs without  $R_*$  in the database, we adopt Mann et al. (2015) calibrations to determine the stellar radius. With a green shadow, we highlight the region with  $d \leq 20$  pc, calling attention to the opportunity provided by the nearby M-dwarf exoplanetary systems. The symbols follow the same notation of Figure 3 (left panel), with the addition of small-dot systems where the exoplanet density is not measured. The M dwarfs closer than 20 pc that host planets without measured densities are shown as upside down triangles. Ross 128b is also presented as blue crosses. We leave the water and gaseous planets as background symbols. From Figure 3 (top right panel) the exoplanets with the lower degree of insolation flux orbit M-dwarf stars (yellow squares and triangles). In contrast, the rocky exoplanets around solar-like stars tend to receive much more flux, generally 1000 times more than the Earth.

In summary, our precise spectroscopic atmospheric parameters and individual abundances have allowed us to use theoretical models to study the potential interior composition of Ross 128b. Assuming Ross 128b formed with the same composition as its host star we calculate its mineralogy, structure, and thus its mass. Our model assumes no atmosphere



**Figure 3.** Left panel: the exoplanet mass–radius diagram using the planetary composition based on Zeng et al. (2016) relations. Exoplanets around M dwarfs are shown with orange squares, and the other stars hosting exoplanets are shown with orange circles. Right panels: the metallicity–distance diagram; in the top panel, we plot the computed insolation flux at the planet’s distance from the star, and in the bottom panel, we adopt the planet’s equilibrium temperature in the color bar. The symbols follow the same notation from the left panel with the addition of upside down triangles for the M dwarfs that are closer than 20 pc from the Sun and host exoplanets without density measurements. We use dots to indicate the stars hosting exoplanets without density measured.

is present, however, because the addition of this layer (or the addition of light elements to the core) would decrease the density for a given radius, our calculated masses represent the *maximum* mass of Ross 128b in the absence of any mantle stripping due to large impacts. In this scenario, if Ross 128 is also depleted in Si relative to Solar we calculate Ross 128b would have a relatively larger core than the Earth, regardless of the mantle chemistry. It is a likely scenario given the relative depletion of alpha-elements in Ross 128. The derived planetary parameters  $S_{\text{Earth}} = 1.79 \pm 0.26$  and  $T_{\text{eq}} = 294 \pm 10$  K support the Bonfils et al. (2017) findings that Ross 128b is a temperate exoplanet in the inner edge of the habitable zone.

K.C. and V.S. acknowledge that their work here is supported, in part, by the National Aeronautics and Space Administration under Grant 16-XRP16\\_2-0004, issued through the Astrophysics Division of the Science Mission Directorate. D.A.G.H., O.Z., and T.M. acknowledge support provided by the Spanish Ministry of Economy and Competitiveness (MINECO) under grant AYA-2017-88254-P. S.R.M. acknowledges support from NSF grant AST-1616636. B.R-A acknowledges the support from CONICYT PAI/CONCURSO NACIONAL INSERCIÓN EN LA ACADEMIA, CONVOCATORIA 2015 79150050. H.J. acknowledges support from the Crafoord Foundation and Stiftelsen Olle Engkvist Byggmästare. J.K.T. acknowledges support for this work provided by NASA through Hubble Fellowship grant HST-HF2-51399.001 awarded by the Space Telescope Science Institute, which is operated by the

Association of Universities for Research in Astronomy, Inc., for NASA, under contract NAS5-26555.

This research has made use of the NASA Exoplanet Archive, which is operated by the California Institute of Technology, under contract with the National Aeronautics and Space Administration under the Exoplanet Exploration Program.

Funding for the Sloan Digital Sky Survey IV has been provided by the Alfred P. Sloan Foundation, the U.S. Department of Energy Office of Science, and the Participating Institutions. SDSS-IV acknowledges support and resources from the Center for High-Performance Computing at the University of Utah. The SDSS web site is [www.sdss.org](http://www.sdss.org).

SDSS-IV is managed by the Astrophysical Research consortium for the Participating Institutions of the SDSS Collaboration including the Brazilian Participation Group, the Carnegie Institution for Science, Carnegie Mellon University, the Chilean Participation Group, the French Participation Group, Harvard-Smithsonian Center for Astrophysics, Instituto de Astrofísica de Canarias, The Johns Hopkins University, Kavli Institute for the Physics and Mathematics of the Universe (IPMU)/University of Tokyo, Lawrence Berkeley National Laboratory, Leibniz Institut für Astrophysik Potsdam (AIP), Max-Planck-Institut für Astronomie (MPIA Heidelberg), Max-Planck-Institut für Astrophysik (MPA Garching), Max-Planck-Institut für Extraterrestrische Physik (MPE), National Astronomical Observatory of China, New Mexico State University, New York University, University of Notre Dame, Observatório Nacional/MCTI, The Ohio State University, Pennsylvania State University, Shanghai Astronomical Observatory, United Kingdom Participation

Group, Universidad Nacional Autónoma de México, University of Arizona, University of Colorado Boulder, University of Oxford, University of Portsmouth, University of Utah, University of Virginia, University of Washington, University of Wisconsin, Vanderbilt University, and Yale University.

*Facilities:* Sloan, NASA Exoplanet Archive.

*Software:* ExoPlex (Unterborn et al. 2018), Turbospectrum (Alvarez & Plez 1998; Plez 2012), MARCS (Gustafsson et al. 2008), PHOENIX BT-Settl (Allard et al. 2013).

### ORCID iDs

Diogo Souto  <https://orcid.org/0000-0002-7883-5425>

Cayman T. Unterborn  <https://orcid.org/0000-0001-8991-3110>

Kevin Covey  <https://orcid.org/0000-0001-6914-7797>

Keivan Stassun  <https://orcid.org/0000-0002-3481-9052>

J. A. Johnson  <https://orcid.org/0000-0001-7258-1834>

Steven R. Majewski  <https://orcid.org/0000-0003-2025-3147>

Henrik Jönsson  <https://orcid.org/0000-0002-4912-8609>

Steven Gilhool  <https://orcid.org/0000-0002-3230-3052>

Cullen Blake  <https://orcid.org/0000-0002-6096-1749>

Felipe Santana  <https://orcid.org/0000-0002-4023-7649>

### References

- Abolfathi, B., Aguado, D. S., Aguilar, G., et al. 2018, *ApJS*, **235**, 42
- Allard, F., Homeier, D., Freytag, B., et al. 2013, *MSAIS*, **24**, 128
- Alvarez, R., & Plez, B. 1998, *A&A*, **330**, 1109
- Anglada-Escudé, G., Amado, P. J., Barnes, J., et al. 2016, *Natur*, **536**, 437
- Asplund, M., Grevesse, N., & Sauval, A. J. 2005, in *ASP Conf. Ser.* 336, Cosmic Abundances as Records of Stellar Evolution and Nucleosynthesis, ed. T. G. Barnes III & F. N. Bash (San Francisco, CA: ASP), 25
- Batalha, N. M., Rowe, J. F., Bryson, S. T., et al. 2013, *ApJS*, **204**, 24
- Benz, W., Slatery, W. L., & Cameron, A. G. W. 1988, *Icar*, **74**, 516
- Blanton, M. R., Bershady, M. A., Abolfathi, B., et al. 2017, *AJ*, **154**, 28
- Bond, J. C., O'Brien, D. P., & Lauretta, D. S. 2010, *ApJ*, **715**, 1050
- Bonfils, X., Astudillo-Defru, N., Díaz, R., et al. 2017, arXiv:1711.06177
- Bonfils, X., Delfosse, X., Udry, S., et al. 2005, *A&A*, **442**, 635
- Charbonneau, D., & Deming, D. 2007, arXiv:0706.1047
- Delfosse, X., Forveille, T., Ségransan, D., et al. 2000, *A&A*, **364**, 217
- Delgado Mena, E., Israelian, G., González Hernández, J. I., et al. 2010, *ApJ*, **725**, 2349
- Dorn, C., Hinkel, N. R., & Venturini, J. 2017, *A&A*, **597**, A38
- Driscoll, P., & Olson, P. 2011, *Icar*, **213**, 12
- Gaia Collaboration, Brown, A. G. A., Vallenari, A., et al. 2018, arXiv:1804.09365
- Gaidos, E., Conrad, C. P., Manga, M., & Hernlund, J. 2010, *ApJ*, **718**, 596
- Gilhool, S. H., Blake, C. H., Terrien, R. C., et al. 2018, *AJ*, **155**, 38
- Gillon, M., Triaud, A. H. M. J., Demory, B.-O., et al. 2017, *Natur*, **542**, 456
- Gunn, J. E., Siegmund, W. A., Mannery, E. J., et al. 2006, *AJ*, **131**, 2332
- Gustafsson, B., Edvardsson, B., Eriksson, K., et al. 2008, *A&A*, **486**, 951
- Jontof-Hutter, D., Rowe, J. F., Lissauer, J. J., Fabrycky, D. C., & Ford, E. B. 2015, *Natur*, **522**, 321
- Lindgren, S., & Heiter, U. 2017, *A&A*, **604**, A97
- Lodders, K. 2003, *ApJ*, **591**, 1220
- Majewski, S. R., Schiavon, R. P., Frinchaboy, P. M., et al. 2017, *AJ*, **154**, 94
- Mann, A. W., Feiden, G. A., Gaidos, E., Boyajian, T., & von Braun, K. 2015, *ApJ*, **804**, 64
- Marcus, R. A., Sasselov, D., Hernquist, L., & Stewart, S. T. 2010, *ApJL*, **712**, L73
- McDonough, W. F. 2003, *TrGeo*, **2**, 568
- Muirhead, P. S., Becker, J., Feiden, G. A., et al. 2014, *ApJS*, **213**, 5
- Nidever, D. L., Holtzman, J. A., Allende Prieto, C., et al. 2015, *AJ*, **150**, 173
- Nordlander, T., & Lind, K. 2017, *A&A*, **607**, A75
- Önehag, A., Heiter, U., Gustafsson, B., et al. 2012, *A&A*, **542**, A33
- Plez, B. 2012, Turbospectrum: Code for Spectral Synthesis, Astrophysics Source Code Library, ascl:1205.004
- Quintana, E. V., Barclay, T., Raymond, S. N., et al. 2014, *Sci*, **344**, 277
- Rojas-Ayala, B., Covey, K. R., Muirhead, P. S., & Lloyd, J. P. 2012, *ApJ*, **748**, 93
- Santos, N. C., Adibekyan, V., Dorn, C., et al. 2017, *A&A*, **608**, A94
- Schmidt, S. J., Wagoner, E. L., Johnson, J. A., et al. 2016, *MNRAS*, **460**, 2611
- Shetrone, M., Bizyaev, D., Lawler, J. E., et al. 2015, *ApJS*, **221**, 24
- Shields, A. L., Ballard, S., & Johnson, J. A. 2016, *PhR*, **663**, 1
- Souto, D., Cunha, K., García-Hernández, D. A., et al. 2017, *ApJ*, **835**, 239
- Souto, D., Cunha, K., Smith, V., et al. 2016, *ApJ*, **830**, 35
- Stassun, K. G., Collins, K. A., & Gaudi, B. S. 2017, *AJ*, **153**, 136
- Thiaud, A., Marboeuf, U., Alibert, Y., Léya, I., & Mezger, K. 2015, *A&A*, **580**, A30
- Unterborn, C. T., Desch, S. J., Hinkel, N. R., & Lorenzo, A. 2018, *NatAs*, **2**, 297
- Unterborn, C. T., Dismukes, E. E., & Panero, W. R. 2016, *ApJ*, **819**, 32
- Unterborn, C. T., & Panero, W. R. 2017, *ApJ*, **845**, 61
- Wilson, J. C., Hearty, F., Skrutskie, M. F., et al. 2010, *Proc. SPIE*, **7735**, 77351C
- Zasowski, G., Cohen, R. E., Chojnowski, S. D., et al. 2017, *AJ*, **154**, 198
- Zeng, L., Sasselov, D. D., & Jacobsen, S. B. 2016, *ApJ*, **819**, 127